Available online at www.sciencedirect.com
ScienceDirect
Trans. Nonferrous Met. Soc. China 33(2023) 3685−3698
Transactions of Nonferrous Metals Society of China
www.tnmsc.cn

Microstructure evolution and mechanical properties of Ti-1023 alloy during β slow cooling process

Hui MING, Cheng-peng ZHU, Xue-yan SONG, Xiao-yong ZHANG, Ke-chao ZHOU

State Key Laboratory of Powder Metallurgy, Central South University, Changsha 410083, China

Received 17 June 2022; accepted 28 October 2022

Abstract: Microstructure evolution and mechanical properties of Ti-1023 alloy during cooling from single-phase region to dual-phase region with the cooling rate of 1 °C/min were systematically investigated. As the final cooling temperature decreased, grain boundary α' martensite (α'_{GB}), grain boundary α phase (α_{GB}), Widmanstatten grain boundary α phase (α_{WGB}), and Widmanstatten intragranular α phase (α_{WI}) were sequentially precipitated. Correspondingly, mechanical properties and deformation mechanisms of Ti-1023 alloy changed significantly. When the final cooling temperature was higher than 700 °C, tensile curve showed an obvious double-yielding phenomenon with elongation >20%. Whereas the final cooling temperature was lower than 700 °C, and the double-yielding phenomenon disappeared. This was mainly attributed to the fact that β stability of Ti-1023 alloys was enhanced with the increase of $\alpha(\alpha')$ precipitated phases. And the room temperature deformation mechanism gradually changed from stress-induced α'' martensitic phase transformation to dislocation slip. Furthermore, strengthening mechanism of Ti-1023 alloy was analyzed in combination with grain size and precipitated phase effects.

Key words: Ti-1023 alloy; microstructure evolution; grain boundary α' martensite; heat treatment

1 Introduction

Titanium and its alloys are increasingly attracting attention due to their low density, high specific strength, low thermomechanical processing cost, good hardenability, and excellent formability [1−3]. Among them, metastable β titanium alloys constitute one of the most versatile groups, with applications including engine components, orthopedic and dental implants, etc. Ti-1023 alloy, a classic metastable β titanium alloy, is widely used as structural components of Boeing series aircraft, due to its good combination of high strength and fracture toughness [4−6].

It is well known that the mechanical properties of titanium alloys depend on their microstructures while the latter was closely related to the thermo-mechanical and heat treatment processes [7−10]. For the thermomechanical process, the effect of processing parameters (including processing temperature, strain rate, etc.) on microstructure and mechanical properties of alloys has been widely reported [11,12]. On the other hand, the heat treatment process is another important factor to determine the microstructure of alloys. For example, ZHANG et al [13] uncovered that with the increase in heating rate of Ti−6Al−4V alloy, the volume fraction of primary α phase (α_p) increased and more secondary α phase (α_s) precipitated in β matrix, and these would affect the final mechanical properties of the alloy.

Besides the heating stage, the parameters in the cooling stage of heat treatment process also play an important role in the microstructure evolution and mechanical properties of titanium alloys. In general, when the titanium alloy is rapidly cooled from high temperatures, a large number of β phases

Corresponding author: Xiao-yong ZHANG, Tel: +86-13975809204, E-mail: zhangxiaoyong@csu.edu.cn
DOI: 10.1016/S1003-6326(23)66363-0

are retained due to the restricted diffusion of alloy elements, and part of β phases may transform to martensite, finally forming the heterogeneous microstructure of martensite and metastable β matrix [14]. While the titanium alloy is cooled from high temperature at a relatively slow rate, some diffusion transformation might occur, the grain boundary α phase (α_{GB}), Widmanstatten grain boundary α phase (α_{WGB}), and Widmanstatten intragranular α phase (α_{WI}) gradually precipitate and grow by decomposing the metastable β matrix, finally forming a stable α phase and residual β matrix coexisting microstructure [15,16]. MAHENDER et al [17] investigated the microstructures and mechanical properties of near α titanium alloy IMI 834 at different cooling rates, they found that with the decrease of cooling rate, the β grain size and the thickness of α lamellar increased, while the strength of the alloy decreased. WU et al [18] found bi-lamellar, basket-weave, and metastable-β microstructures formed in Ti-5321 alloy with the cooling rate increasing. Compared with fast cooling, titanium alloy undergoes a more complex microstructure evolution during slow cooling processes, which has a greater effect on the mechanical properties of the alloy. SUN et al [19] investigated four stages of microstructure evolution when TA15 alloy is slowly cooled from high temperatures, including nucleation of α_{GB} phase, growth of α_{GB} phase, nucleation of α_{WGB} phase, and growth of α_{WGB} phase. TANG et al [20] investigated the nucleation mode of α_{WGB} lamellar in Ti-7333 alloy during β slow cooling process, and found that the α_{WGB} phase could not only grow up from α_{GB} grains by inheriting the orientations but also sympathetically nucleate at the α_{GB}/β interface. These works provide good support for studying the phase transformation sequences and microstructure evolution of different titanium alloys during β slow cooling. However, up to now, few studies have focused on the effect of these precipitated phases on the mechanical properties of the alloys and their roles in the deformation.

In this work, six different samples of Ti-1023 alloy were cooled from single-phase region to different final cooling temperatures. Their microstructures, mechanical properties, and deformation modes were carefully compared. The microstructural evolution of Ti-1023 alloy during the slow cooling process was systematically investigated. The effect of grain boundary precipitated phases on the mechanical properties of the alloys and their roles in deformation were evaluated. This work provides an experimental basis for designing heat treatment routes for Ti-1023 alloy and provides a reference for controlling microstructure and optimizing the mechanical property of the metastable β titanium alloy.

2 Experimental

A forged Ti-1023 alloy billet provided by Hunan Goldsky Titanium Industry Technology Co., Ltd., China, with a chemical composition (wt.%) of 2.91 Al, 9.75 V, 1.81 Fe, and Ti (balance) was used in this study. The original microstructure of this billet is shown in Fig. 1(a). The α/β transformation temperature (T_β) of this billet is (810±10) °C by using the metallographic method and thermal analysis.

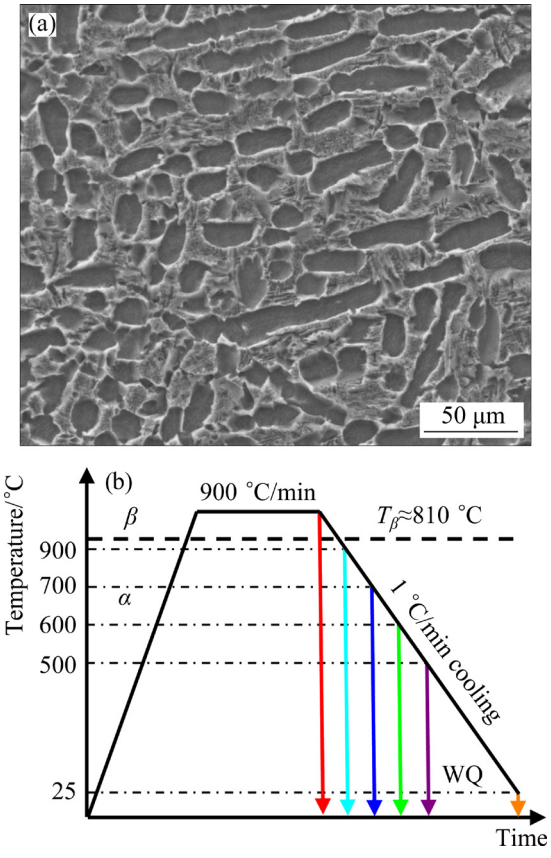

Fig. 1 Original microstructure of as-received Ti-1023 alloy billet (a), and schematic diagram of heat treatment route (b)

Some small samples cut from the forged billet were solution treated at 900 °C for 2 h. Then, these samples were cooled in the furnace at a controlled

cooling rate of 1 °C/min, followed by water quenching after reaching a prescribed temperature of 900, 800, 700, 600, 500 °C, and room temperature (25 °C), respectively. These obtained samples are named SC900, SC800, SC700, SC600, SC500, and SC25, respectively. The heat treatment routes are shown in Fig. 1(b).

Some small blocks were cut from the core of the heat-treated samples for the microstructure characterization, and then these small blocks were mechanically ground and electrochemically polished in the Kroll's solution (60% methanol, 35% butanol, and 5% perchloric) for 25 s. Scanning electron microscopy (SEM) and electron backscatter diffraction (EBSD) observation were conducted on TESCAN MIRA3 (FEI, Czech Republic) electron microscopy equipped with an EDAX detector, and the electron probe microanalysis (EPMA) was conducted on a JXA−8530F (Japan) electron microscopy. Thin foils for transmission electron microscopy (TEM) were prepared by using a twin-jet electrolytic apparatus (Denmar Struers A/S, Denmark) electropolished at −23 °C with Kroll's solution. As to the samples for mechanical properties testing, dog-bones tensile specimens with gauge dimensions of 26 mm × 10 mm × 1.5 mm were cut from the heat-treated samples, and tensile tests were carried out by using a CMT4204 mechanical testing machine (SUST, China). The size of β grains and the content of the α phase were statistically analyzed by using Image J software.

3 Results

3.1 Initial microstructures

Figure 2 shows the microstructure of the SC900 sample. In this condition, the sample exhibits a typical microstructure with randomly oriented β grains, and the average grain size is ~283 μm, as shown in Fig. 2(a). Figure 2(b) shows a straight and clear grain boundary in the TEM bright field (BF) image. And the inset in Fig. 2(b) presents the selected area electron diffraction (SAED) pattern taken from $[\bar{1}13]_\beta$ zone axis of the right grain. Besides, the distinct diffraction of the β matrix, some additional diffraction spots at 1/3 and 2/3$\{11\bar{2}\}_\beta$ positions can be observed, indicating the formation of athermal ω phase within the β grains. This is expected as the solution temperature is higher than the β-transus temperature (~810 °C) and the phase stability of Ti-1023 alloy is not sufficiently high to inhibit the formation of athermal ω phase during water quenching. This result is also similar to that of some other metastable β titanium alloys [21,22].

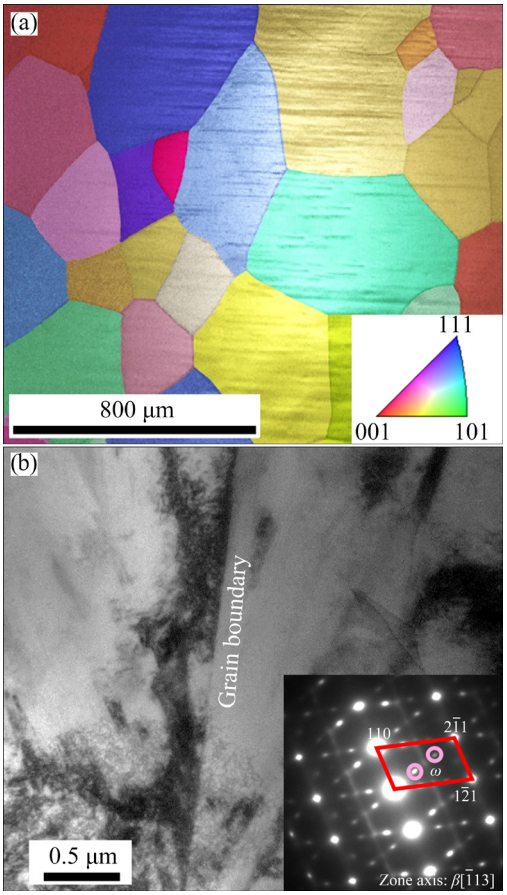

Fig. 2 Microstructures of SC900 sample: (a) Inverse pole figure (IPF) map; (b) TEM image at grain boundary and corresponding selected area electron diffraction (SAED) pattern along $[\bar{1}13]_\beta$ zone axis

Figure 3 shows the microstructure of the SC800 sample. As seen in Fig. 3(a), majority of β phases are retained inside the grain, and few precipitated phases can be seen in the interior of the grain. However, many fine needle-like phases precipitated near the grain boundaries, which is different from that in the SC900 sample. A similar microstructure has also been reported in a previous study in Ti-1023 alloy, and it is recognized as α'' martensite [23]. However, further characterization in our study suggests that these precipitated phases might not have orthogonal lattice structures. As shown in Fig. 3(b), a typical triangular grain boundary with precipitated phases was selected for

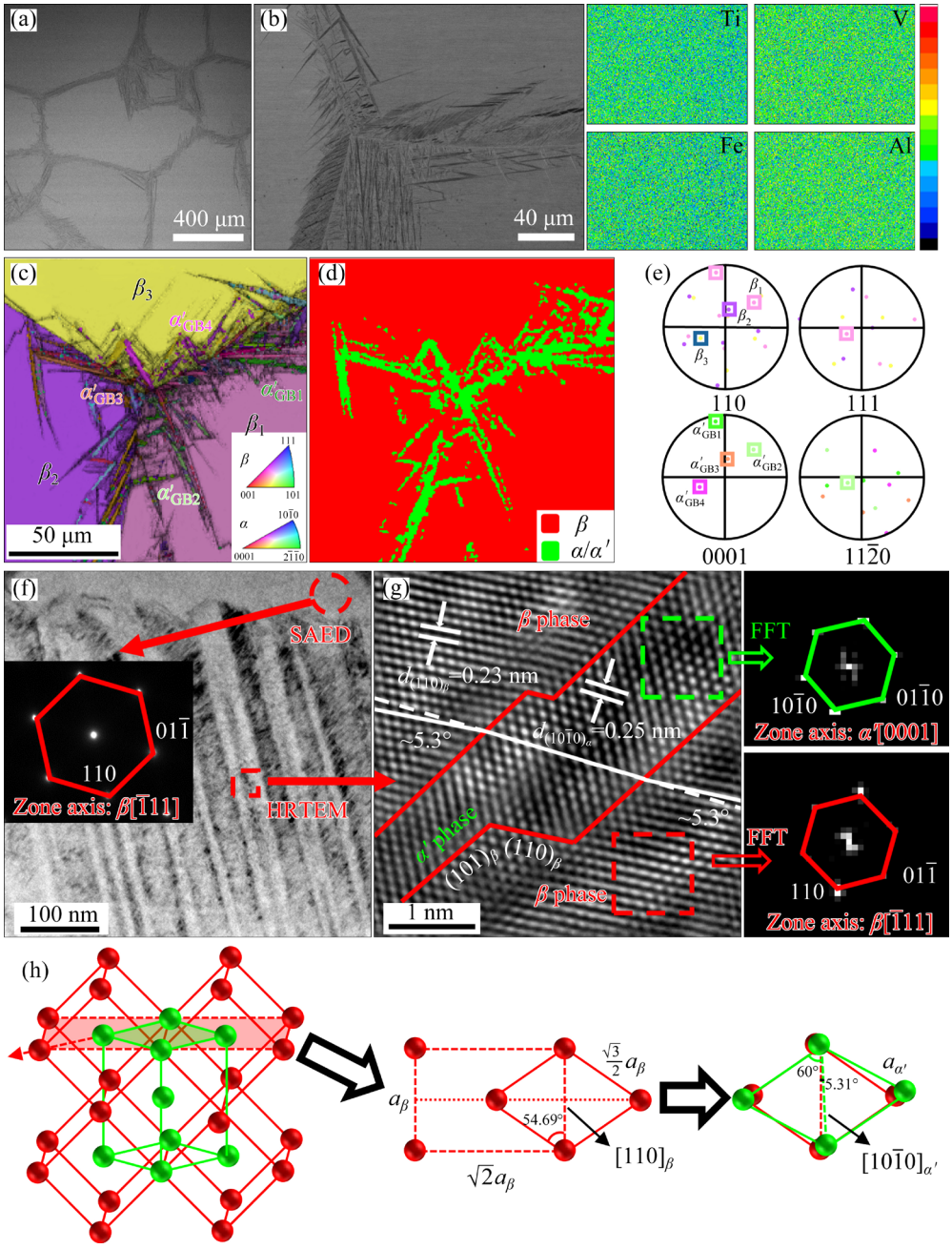

Fig. 3 Microstructures of SC800 sample: (a) Low magnification SEM image; (b) EPMA image; (c) EBSD IPF map at grain boundary; (d, e) Corresponding phase map and PF of selected α'_{GB} and β phases, respectively; (f) TEM image and corresponding SAED pattern at grain boundary; (g) HRTEM image corresponding to red dashed rectangle in (f); (h) Schematic of $\beta \rightarrow \alpha'$ transition

elemental analysis. Interestingly, the composition between the phase precipitated near the grain boundary and β matrix was almost the same, without visible elemental segregation. In other words, this is not traditionally thought of α_{GB}. Furthermore, the crystal structure analysis by EBSD shows that the precipitated phases have the same hexagonal close-packed (HCP) structure as α phase (Fig. 3(d)). The phase structure transition from body centered cubic (BCC) to HCP implies that a $\beta \rightarrow \alpha'$ martensitic phase transformation may occur near the grain boundaries during water quenching in this condition, since α' martensitic phase and α phase have an identical crystal structure and lattice parameters. Figures 3(c) and (e) exhibit the crystallographic orientation relationship between grain boundary α' martensite phase (α'_{GB}) and β phase by IPF map and pole figure (PF). As can be

seen, there are different orientations in different α'_{GB}. We selected four α'_{GB} with different orientations and analyzed the orientation relationships between them and β matrix. All the four α'_{GB} meet $\{0001\}\alpha'_{GB}//\{110\}_{\beta}$, i.e., Burgers orientation relationship (BOR). Furthermore, TEM observations were used to characterize the more microscopic morphology of the precipitated phases. Figure 3(f) shows the morphology of the α'_{GB} in TEM bright field image. As shown in SAED pattern of the insert figure, the β grain was taken from $[\bar{1}11]$ zone axis. Figure 3(g) shows a high-resolution TEM (HRTEM) image of the red dashed rectangle in Fig. 3(f). Two different atomic configurations refer to α' martensite phase and β phase, respectively. Plane spacings of $(110)_{\beta}$ and $(10\bar{1}0)_{\alpha'}$ are measured to be 0.23 and 0.25 nm, and the $(10\bar{1}0)_{\alpha'}$ lattice planes have angles of approximately 5.3° deviating from $(110)_{\beta}$. Figure 3(h) shows the changes in atomic arrangement of titanium alloy during $\beta\rightarrow\alpha'$ transition, and it can be seen that there is an angle of 5.31° between $(110)_{\beta}$ and $(10\bar{1}0)_{\alpha'}$, which is consistent with what observed in Fig. 3(g). Note that the α' martensite is rarely reported in Ti-1023 alloy. Herein, a reasonable speculation is that the overlapping of stacking faults promotes the precipitation of martensite, when the β grain size is sufficiently large [24].

Figure 4 shows the microstructure of the SC700 sample. As shown in Fig. 4(a), some phases with distinct protrusions and darker colors precipitated at the grain boundaries, and some fine needle-like phases precipitated near the grain boundaries, which is similar to that in the SC800

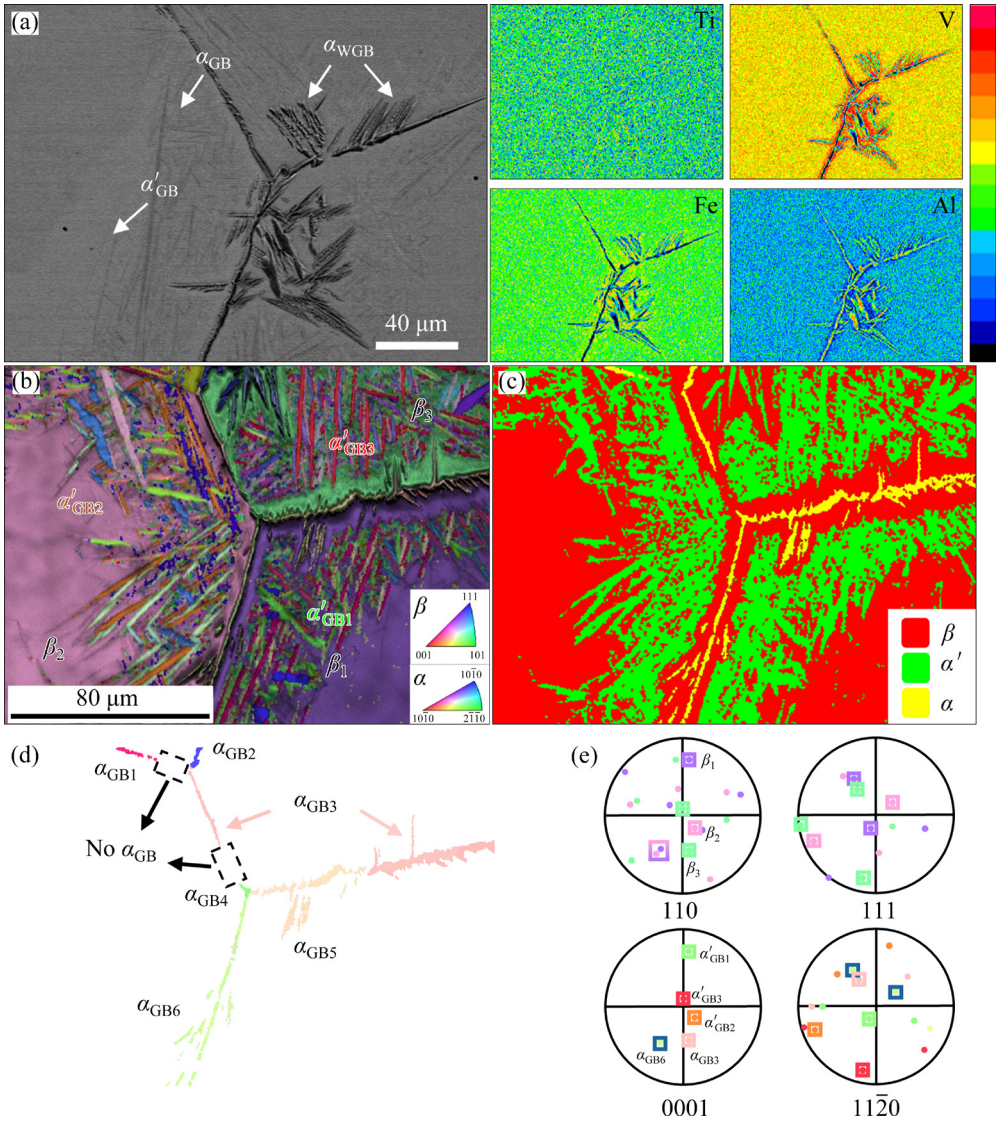

Fig. 4 Microstructures of SC700 sample: (a) EPMA image at grain boundary; (b) IPF map; (c) Corrected phase map; (d) IPF map of selected α_{GB1}–α_{GB6}; (e) Corresponding PF of α'_{GB}, α_{GB} and β phases

sample. The elemental analysis by EPMA shows that the fine needle-like phases precipitated near the grain boundaries have the same composition as the β matrix, suggesting that they are the same α' phase as that in the SC800 samples. However, the dark precipitated phases show obvious element segregation compared with β matrix. These phases have more α-stable elements (Al) but fewer β-stable elements (V and Fe), which can be inferred as α phase. Furthermore, they can be distinguished into α_{GB} and α_{WGB} according to their positions. In addition, the most β-stable elements and the fewest α-stable elements are enriched and precipitate-free zones are formed nearing the α_{GB} and α_{WGB} (Fig. 4(a)). It has been widely reported that $\beta\rightarrow\alpha$ transformation belongs to diffusional transition. Wherein α-stable elements (Al) are enriched into α phase or make a new α nuclei, and the β-stable elements (V and Fe) diffuse out of the α phase and are enriched in the adjacent zone [25]. Figure 4(b) shows many α'_{GB} with different orientations, and they all maintain a BOR with β matrix (Fig. 4(e)), as mentioned in the SC800 samples. Different α_{GB} precipitates are extracted and illustrated in Fig. 4(d), which can be seen that the grain boundaries mainly exhibit the following three states: (1) No α_{GB}: No precipitation of α phase at the grain boundary, the β grains are contacted directly, as marked with black dashed rectangles in Fig. 4(d); (2) Discontinuous α_{GB}: Several different orientations of α_{GB} alternately are precipitated at the same grain boundary, such as α_{GB3} and α_{GB5} between β_1 and β_3 grains; (3) Continuous α_{GB}: Single oriented α_{GB} is precipitated continuously at the grain boundary, such as the α_{GB6} between β_1 and β_2 grains. These three different states of α_{GB} are mainly due to the fact that α_{GB} is precipitated as spherical particles, followed by variant selection according to crystallographic adaptation, and different α_{GB} variants grow at different rates during the cooling process [26]. Therefore, there are three cases of no α_{GB}, single α_{GB} variant, or multiple α_{GB} variants covering the grain boundaries during cooling process. Furthermore, the α_{GB3} and α_{GB6} were selected to analyze the orientation relationship of α_{GB} and β grains. The PF in Fig. 4(e) indicates that α_{GB3} only keeps BOR with β_3 and shows a weak relationship with β_1. However, α_{GB6} shows BOR with β_1 and β_2 grains simultaneously, $\{0001\}\alpha_{GB6}//\{110\}_{\beta_1}//\{110\}_{\beta_2}$, as these two β grains have a set of parallel $\{110\}$ planes. It is suggested that the α_{GB} maintains BOR with one or two adjacent β grains.

When step cooling to 600, 500, and 25 °C, it can be seen from Fig. 5 that the grain boundaries are completely covered by α phase, and many lamellar α phases are precipitated inside the grains. The contents of α phase were determined to be 56%, 64%, and 65%, respectively, according to the statistics results by Image J software. These results clarify that the α phases are gradually precipitated and grow during step cooling process, and majority

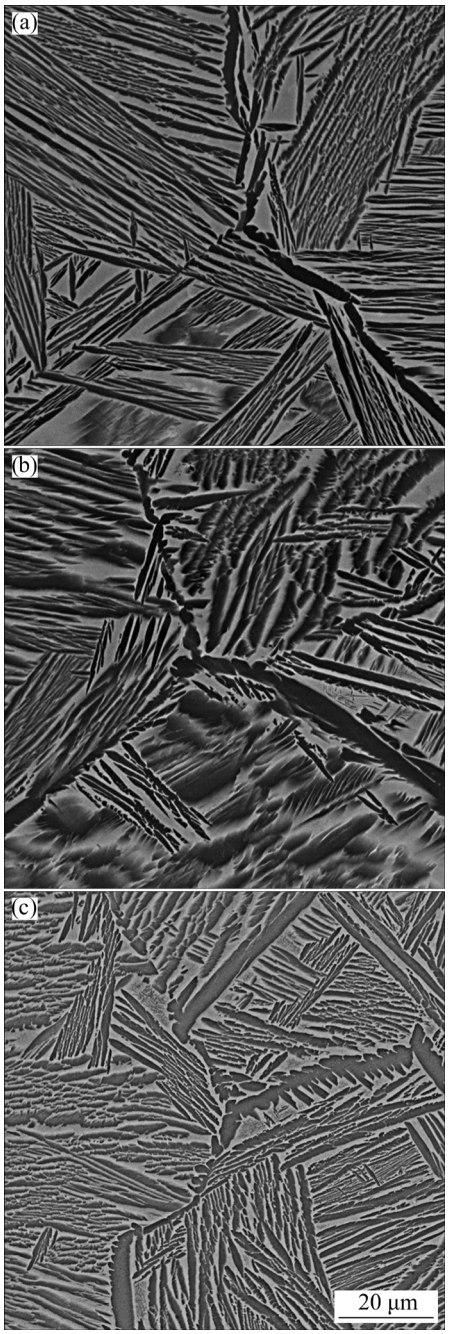

Fig. 5 SEM images at grain boundary of SC600 (a), SC500 (b), and SC25 (c) samples

of the α phases are precipitated when cooling to 500 °C, as the weak difference in microstructure between the SC500 and SC25 samples. Some fine needle-like α phases precipitated in the residual β matrix were observed in the SC500 and SC25 samples, which is absent in other samples. In addition, the thickness of α_{GB} phase also increased with the decrease of quenching temperature.

3.2 Mechanical properties

Tensile tests were carried out on all the samples to evaluate the effect of quenching temperature on the mechanical properties. Figure 6 exhibits representative stress−strain curves of different samples and correlation of ultimate tensile strength (UTS) and elongation with final slow cooling temperature. It can be seen that typical double-yielding phenomena are exhibited in the stress−strain curves of SC900, SC800, and SC700 samples, and these samples show better plasticity and lower strength compared with other samples. This is probably because when the quenching temperature is higher than 700 °C, the microstructures of the alloy are mainly β phase with low β stability, and stress-induced martensite transformation occurs during deformation, finally resulting in the high plasticity of the alloy [27,28], and this phenomenon is also called as transformation induced plastic (TRIP) effect. For these three samples, the UTS and El also show significant difference. Compared with the SC900 sample, the strength of SC800 sample decreased from 845.99 to 790.82 MPa, while its plasticity increased from 21.92% to 35.38%, with an increase of about 61.41%. However, when the quenching temperature is decreased further to 700 °C, the UTS of this alloy increases but El decreases. From the results in Section 3.1, it is reasonable to infer that such a trend is related to the microstructure evolution near grain boundaries. As for the SC600, SC500 and SC25 samples, double-yielding phenomenon is absent, and their strength is higher than that in other samples. In contrast, the El shows a significant decrease as the TRIP effect disappeared with cooling proceeding further. The El in the SC25 sample is decreased by 60.54% compared with that in the SC800 sample. Such a significant difference in El suggested the important role of α phase in deformation.

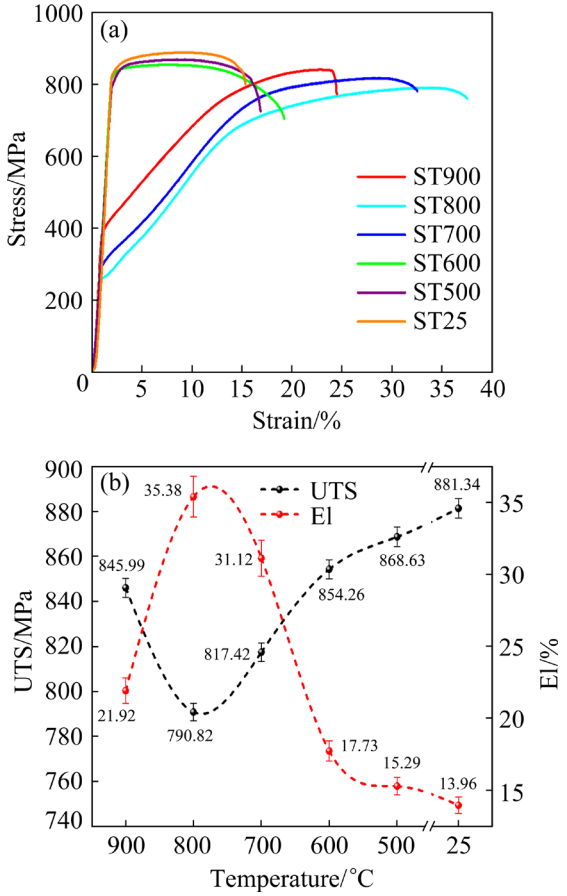

Fig. 6 Mechanical properties of different samples: (a) Stress−strain curve; (b) UTS and El

3.3 Deformed microstructures

To analyze the role of different precipitated phases on tensile deformation, the deformation microstructures in the samples with tensile strains up to 5% were observed by using SEM and TEM, as shown in Figs. 7−11. Figure 7 shows the SEM images of deformation microstructure of the alloy in different cooling conditions. For the SC900 sample, some parallel deformation bands were observed in the matrix (Fig. 7(a)). It is easy to find that they initiated or terminated at grain boundaries, which might cause local stress concentration at grain boundaries or form micro-voids and kinks at grain boundary [29]. As for the SC800 and SC700 samples, deformation bands were also observed in the deformed samples, while these bands initiate or terminate at the pre-precipitated α'_{GB} instead of the grain boundary (Figs. 7(b) and (c)). For the SC25 sample, there were no parallel deformation bands observed in the β matrix, and several small holes appeared at the interface of α and β phases (Fig. 7(d)).

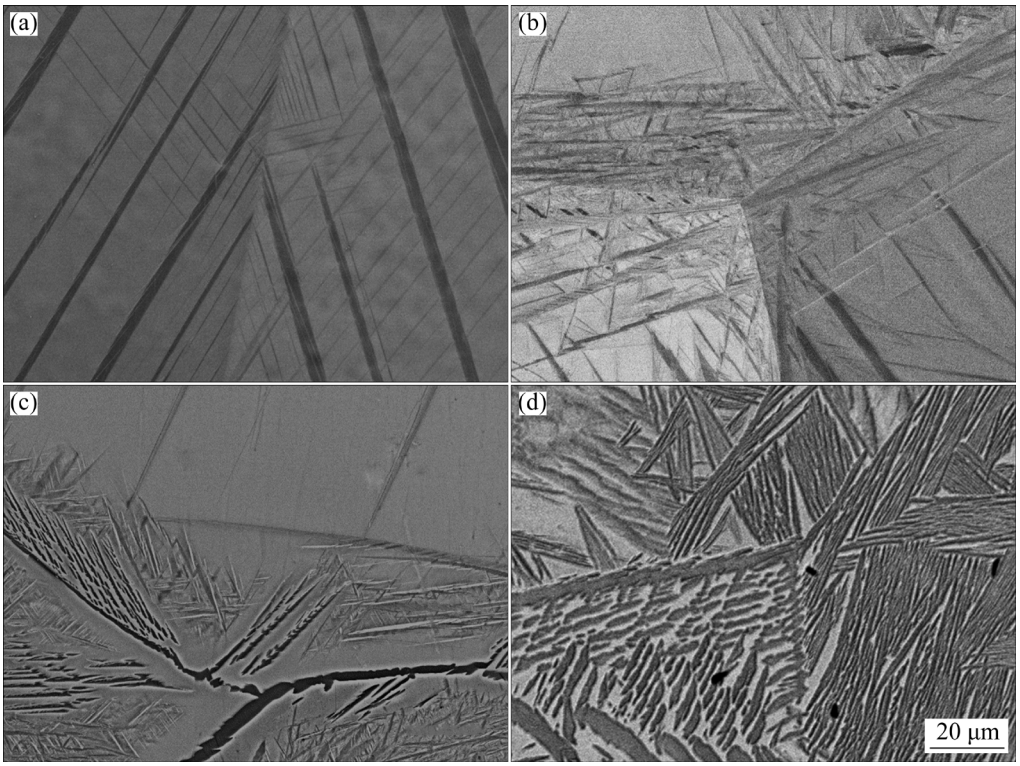

Fig. 7 SEM images at grain boundary of different samples at strain of 5%: (a) SC900; (b) SC800; (c) SC700; (d) SC25

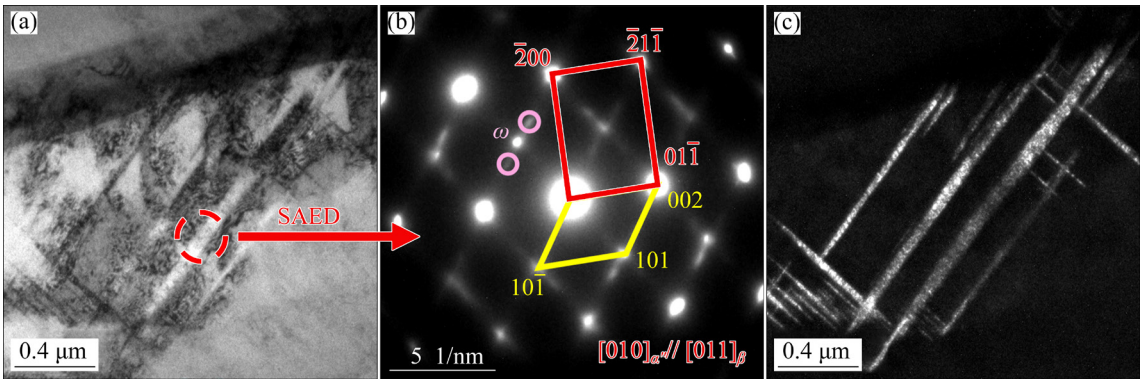

Fig. 8 TEM images of SC900 sample at strain of 5%: (a) BF image; (b) SAED pattern corresponding to red dashed circle in (a); (c) DF image acquired using martensite reflection marked in (b)

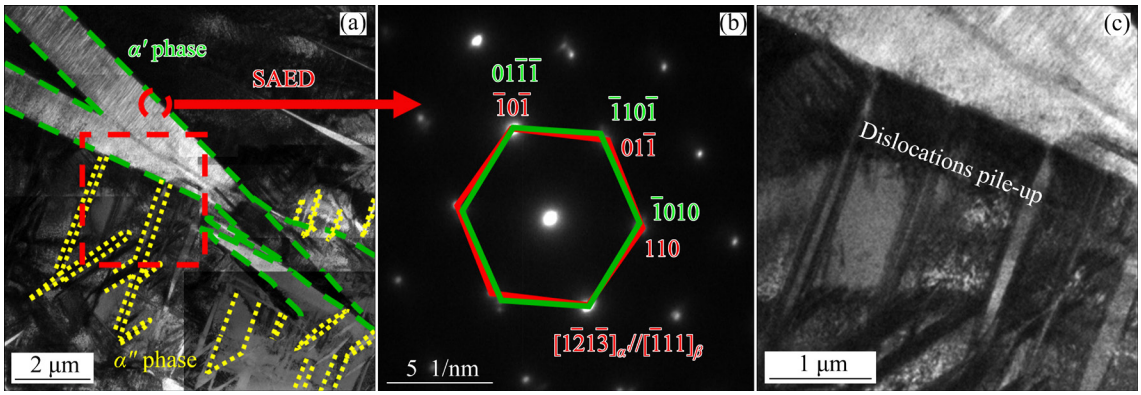

Fig. 9 TEM images of SC800 sample at strain of 5%: (a) BF image; (b) SAED pattern corresponding to red dashed circle in (a); (c) Magnified view corresponding to red dashed rectangle in (a)

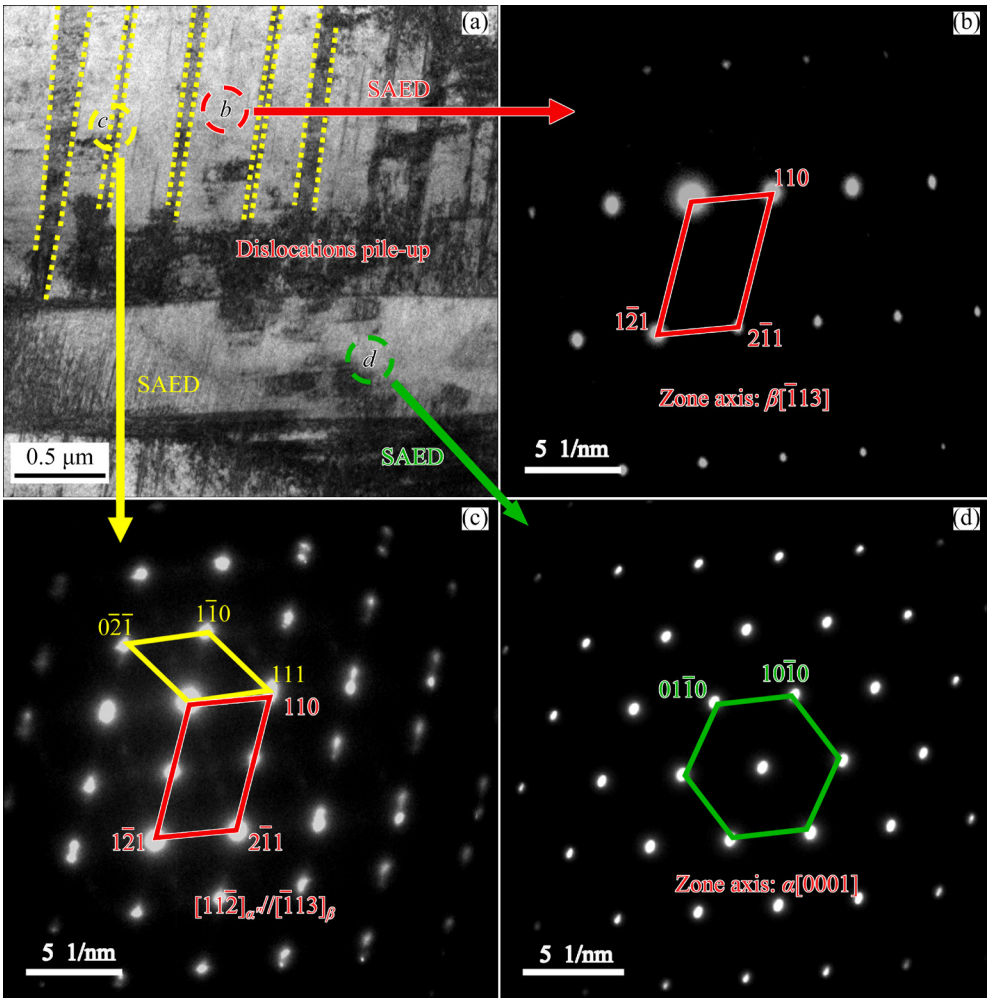

Fig. 10 TEM images of SC700 sample at strain of 5%: (a) BF image; (b−d) SAED patterns corresponding to Regions *b*, *c*, and *d* in (a), respectively

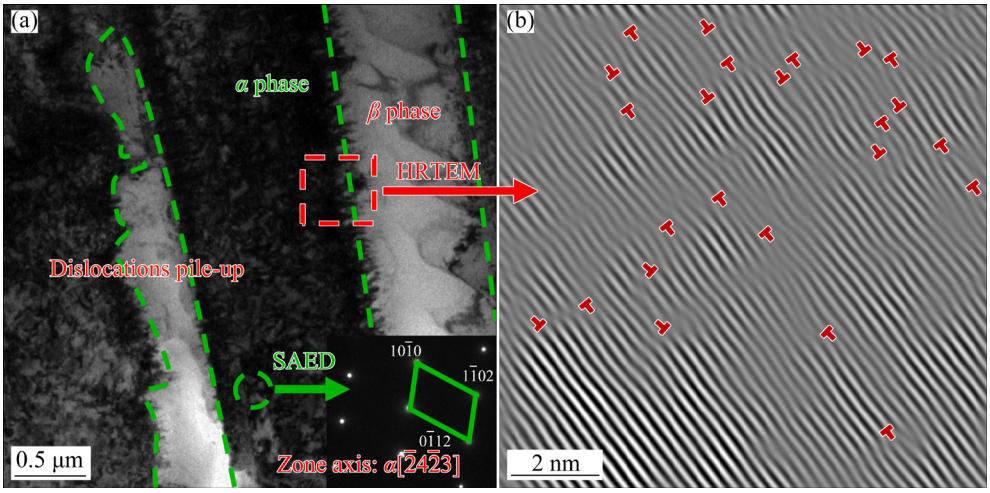

Fig. 11 TEM images of SC25 sample at strain of 5%: (a) BF image and corresponding SAED pattern; (b) HRTEM image corresponding to red dashed rectangle in (a)

To further understand the more microscopic deformation mechanisms in different samples, TEM images in the deformation microstructure were compared. Figure 8(a) shows the BF image of deformation bands in the deformed SC900 sample. According to the associated SAED pattern

(Fig. 8(b)) along $[0\bar{1}0]_{\alpha''}//[011]_{\beta}$ zone axis, these deformation bands can be identified as stress-induced α'' martensite. The presence of stress-induced α'' martensite is more clearly demonstrated by the corresponding dark field (DF) image in Fig. 8(c), and the average width is about 60 nm. In addition, the ω phases still exist in the SAED pattern; however, the diffraction intensity is weaker compared with the initial SC900 sample (Fig. 2(b)), which suggests that some ω phases maybe transform into other phases during deformation. XIAO et al [22] reported that the decrement in the content of ω phase is attributed to the reverse β-to-ω transformation.

Figure 9(a) shows a typical microstructure at grain boundary in the deformed SC800 sample. The phase within the green dashed line can be identified from the SAED pattern (Fig. 9(b)) as α' phase. And the phases within the yellow dashed line are parallel to each other, with two different orientations. According to Fig. 8, it can be easily identified as stress-induced α'' phase. Figure 9(c) shows an enlarged view of the red dashed rectangle in Fig. 9(a). As can be seen, the α' phase hindered the further growth of the stress-induced α'' phase, and many dislocations piled up at the interface of α' and α'' phases.

For the deformed SC700 sample, α and α' phases co-exist, and they can effectively strengthen the grain boundary in deformation. The stress-induced α'' martensite was obstructed by these phases, as shown in Fig. 10(a). Figure 10(b) presents the SAED pattern taken within the red dashed circle in Fig. 10(a), it is easy to know these diffraction spots belong to $[\bar{1}13]$ zone axis of β phase. Figure 10(c) shows the SAED result of the interface between β matrix and deformed bands, which corresponds to the yellow dashed circle in Fig. 10(a). A set of diffraction spots of $[11\bar{2}]_{\alpha''}$ are attached in the pattern of $[\bar{1}13]_{\beta}$ zone axis, indicating that these deformation bands are α'' martensite. Figure 10(d) shows the SAED pattern corresponding to the green dashed circle in Fig. 10(a). It can be found that these diffraction spots are the pattern of α phase along $[0001]_{\alpha}$ zone axis, and it also suggests that the phase in the green circle is the α phase. Thus, it is easy to find that the α phase also prevents the further growth of α'' phase. Moreover, a large number of dislocations piled up around the α phase also can be observed clearly in Fig. 10(a).

Figure 11 shows the TEM image of the deformed SC25 sample. As shown in the insert figure in Fig. 11(a), the SAED pattern indicated that these diffraction spots belong to $[\bar{2}4\bar{2}3]$ zone axis of α phase. As can be seen from Fig. 11(a), lots of dislocations pile-up inside the α phase and at the α/β interface. Figure 11(b) shows HRTEM image of the red dashed rectangle in Fig. 11(a), which confirms the presence of a large number of dislocations. Thus, it is reasonable to infer that the dislocation slip is the most important feature in such microstructures during deformation, and the α/β interface will play an important role in preventing dislocation slip.

4 Discussion

4.1 Microstructure evolution during β slow cooling

The schematic drawing for the microstructure evolution of Ti-1023 alloy during β slow cooling is shown in Fig. 12. As mentioned above, the microstructure of the Ti-1023 alloy was single β phases with an average grain size of ~283 μm after solution treated at 900 °C for 2 h. When the alloy was cooled from 900 to 800 °C, the grain size increased to ~450 μm and some α'_{GB} phase precipitated. JUN and CHOI [30] reported that the coarsening of β grain promoted the formation of α' martensite phase with the increase in the number of nucleation sites (overlapping of stacking faults) of martensite. LEE et al [24] indicated that the overlapping of stacking faults provided the nucleation sites for the martensitic transformation, and the reduction of stacking fault energy (SFE) would promote the martensitic transformation. Therefore, it could be inferred that the formation of α' phases was due to the decrease of SFE with the growth of β grains during cooling, which promoted the formation of martensite in the water quenching. When continued cooling to 700 °C, the alloying elements diffused and the α stable elements gathered at the grain boundary, forming α_{GB} and α_{WGB} phases. In addition, as the consequence of the increase of the β grain size, low SFE still promoted the precipitation of α' phase during water quenching. When further cooled to lower temperatures, the α_{WGB} phase grew up and finally formed lamellar microstructures. In these conditions, since a large

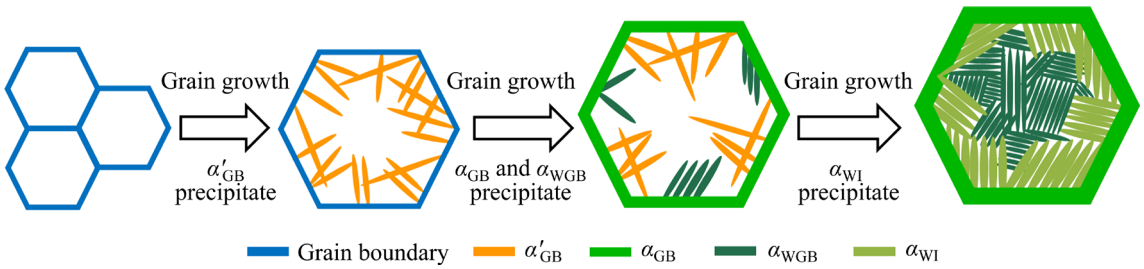

Fig. 12 Schematic diagram of microstructure evolution of Ti-1023 alloy during β slow cooling

number of α stable elements diffused in the α phase, the contents of β stable elements in the β matrix increased, and the β stability increased, there is no α' phase precipitated during water quenching. APPOLAIRE et al [31] reported that when the alloy was cooled from the β phase field at a slow cooling rate, α_{GB} and α_{WGB} phases would precipitate, and the microstructure evolution can be divided into the following stage: (1) the α_{GB} phase nucleated at β grain boundaries as the cooling temperature decreased to $\alpha+\beta$ phase field; (2) the α_{GB} phase grew up and connected with adjacent α_{GB} phase until covering the whole β grain boundaries; (3) the α_{WGB} phase precipitated near the α_{GB} phase and grew into the β grain. In this work, the microstructure evolution of Ti-1023 alloy cooling from 800 to 700 °C at 1 °C/min shows a similar evolution behavior. When cooled from 700 °C to lower temperatures, some α_{WI} precipitated and grew until distributed throughout the β grains, eventually forming a lamellar microstructure.

4.2 Strengthening mechanism

As shown above, the variation of mechanical properties mainly comes from the microstructure evolution during β slow cooling. The strengthening mechanisms of titanium alloys generally include solid solution strengthening, second phase strengthening, α phase lattice strengthening, grain size effect, aging precipitation strengthening, and crystallographic texture strengthening [32,33]. Herein, the β grain size and the precipitated phases are the main reason for the difference in mechanical properties of the different samples.

Based on the above principles, the yield stress of Ti-1023 alloy can be expressed by the following equation [34]:

$$\sigma=\sigma_{\beta}+\sum_{i}\varphi_i\sigma_i \tag{1}$$

where σ_β represents the strength of the β matrix, i refers to the precipitated phase, φ_i represents the volume fraction of phase i, and σ_i is the strength of the precipitated phase i.

The σ_β is related to the average size of β grain by the classical Hall−Petch relationship [35]:

$$\sigma_{\beta}=\sigma_0+k_{\beta}d_{\beta}^{-1/2} \tag{2}$$

where σ_0 and k_β represent the friction stress and Hall−Petch coefficient for β phase, respectively, and d_β is the average diameter of β grain. There is no doubt that the β grain size increases with the increase of slow cooling time. While, the growth rate of β grain is gradually slow with the decreasing temperature during the cooling process. Therefore, although the grain increases, the effect of grain size becomes weaker, particularly when the quenching temperature is lower than 800 °C. In contrast, the effect of precipitated phases on the mechanical properties of alloy is more obvious.

The σ_i can be expressed by the following equation [7]:

$$\sigma_i=\frac{k_0}{\sqrt{\lambda_i}} \tag{3}$$

where k_0 is a material constant, and λ_i is the mean spacing length of precipitated phase. According to this equation, it is known that with the decrease of λ_i, the σ_i increases and its increase rate gets slower.

The variations in mechanical properties of Ti-1023 alloy during cooling can be explained as follows: When the alloy is cooled from 900 to 800 °C, the increase of β grain resulted in the decrease of σ_β and the increase of ductility. In addition, the precipitation of α' martensite increases $\sum_i\varphi_i\sigma_i$; however, this is not sufficient to alter the overall decrease in strength. As a result, the strength of the alloy decreases while the ductility of the alloy increases. When the alloy is cooled to 700 °C,

the β grains continue to grow while the growth rate decreases, which leads to only a little decrease in σ_β. On the other hand, precipitation of the α_{GB} and α_{WGB} phases caused a large increase in $\sum_i \varphi_i \sigma_i$. Therefore, the strength of the alloy increases again. In addition, with the precipitation of the α_{GB} and α_{WGB} phases, the enhanced β stability makes the TRIP effect weaker, resulting in the decrease of ductility. With further cooling, the growth of β grains is difficult to continue, while the massive precipitation of the α phase caused a sharp increase in $\sum_i \varphi_i \sigma_i$. Thus, the strength of the alloy increases sharply. And with the further precipitation of α phase, the deformation mode changes from stress-induced α'' martensite transformation to dislocation slip with increasing β stability, which results in a large reduction of ductility. During further cooling to 25 °C, as the precipitation and growth rate of α phase gets slower, less $\sum_i \varphi_i \sigma_i$ increases, resulting in only a slight increase in the final strength of the alloy.

4.3 Deformation behavior

For the SC900 sample, as can be seen from Fig. 8, martensite phases are produced during deformation, which manifests the TRIP effects, and it may be responsible for high plasticity in this condition. The stress-induced martensite would initiate or terminate at the grain boundaries, and the shear stress that forms the stress-induced martensite may cause the stress concentration at these positions, further resulting in crack nucleation [29]. In addition, as the hard ω particles are difficult to cut through or bypass, dislocations easily pile-up at the ω/β interfaces, and the micro-voids more likely nucleate at these positions [21]. With further increase in the degree of deformation, these micro-voids merge into micro cracks and finally result in the failure of the alloy.

Similarly, for the SC800 and SC700 samples, a large amount of martensite is also introduced during deformation. However, unlike the SC900 sample, the growth of α'' phase is prevented by α'_{GB} and α_{GB}. On the one hand, the amount of α'_{GB} is more than that of grain boundary, so the degree of stress concentration is lower than that in SC900 sample. On the other hand, the atomic arrangement, both at the interfaces of β/α'_{GB} and β/α_{GB}, is more regular than that at β grain boundary, which might result in the dislocation not easily accumulated here. Thus, the plasticity of the SC800 and SC700 samples is better than that of the SC900 sample.

For the SC600, SC500 and SC25 samples, no widespread martensite will be induced and dislocation slip is the most important feature during deformation, while it is easily prevented by α/β interface. The strength of alloy was determined by the combination of the strength of α phase, β phase, and their interface. With the increase in the width of α lamellar, the role of α phase transforms from a single strengthening effect to a combination of strengthening and deformation effect. A large number of dislocations are generated within α and at the α/β interface to coordinate the deformation. As the deformation process proceeds further, local stress concentration will occur at α/β interface, which will form some micro-voids, and eventually lead to the fracture of the alloy.

5 Conclusions

(1) During the slow cooling process of Ti-1023 alloy, the β grains grow up, and when cooling to the temperature near T_β, α'_{GB} phase precipitates after water quenching. Subsequently, α_{GB} and α_{WGB} phases gradually precipitate and grow up. Then, α_{WI} precipitates and finally distributes throughout the β grains, forming a lamellar microstructure.

(2) The mechanical properties of step cooling Ti-1023 alloys are affected by the β grain size, the types and sizes of precipitated phases. With the decrease in quenching temperature during step cooling, the strength of Ti-1023 alloy decreases and then increases, while its ductility shows an opposite trend. The SC800 sample exhibits the highest elongation of ~35.38% with limited UTS of ~790.82 MPa.

(3) With decrease of quenching temperature during step cooling process, the main deformation mode of Ti-1023 alloy would change. When the cooling temperature is not lower than 700 °C, the deformation of the alloy is dominated by the TRIP effect. And when cooling to lower temperature, the deformation of the alloy is dominated by dislocation slip.

Acknowledgments

The authors are grateful for the financial supports from the National Natural Science Foundation of China (No. 51871242), the Innovative Province Construction Special Project

of Hunan, China (No. 2020GK4018), and the Technology Research Project of Hunan Province, China (No. 2021GK1080).

References

[1] MA Xin-kai, LI Fu-guo, CAO Jun, LI Jing-hui, SUN Zhan-kun, ZHU Guang, ZHOU Shun-shun. Strain rate effects on tensile deformation behaviors of Ti−10V−2Fe−3Al alloy undergoing stress-induced martensitic transformation [J]. Materials Science and Engineering A, 2018, 710: 1−9.

[2] CHEN Zhao-qi, XV Li-juan, CAO Shou-zhen, YANG Jian-kai, ZHENG Yun-fei, XIAO Shu-long, TIAN Jing, CHEN Yu-yong. Characterization of hot deformation and microstructure evolution of a new metastable β titanium alloy [J]. Transactions of Nonferrous Metals Society of China, 2022, 32(5): 1513−1529.

[3] ZHANG Hui-yan, LIU Yan-hui, LI Zhi-wei, XIONG An-hui, LI Ke, FU Jia-yun. Crack analysis in Ti−6Al−4V alloy produced by selective laser melting [J]. Tungsten, 2021, 3(3): 361−367.

[4] BOYER R R, BRIGGS R D. The use of β titanium alloys in the aerospace industry [J]. Journal of Materials Engineering and Performance, 2005, 14(6): 681−685.

[5] NIESSEN F, GAZDER A A, MITCHELL D R G, PERELOMA E V. In-situ observation of nucleation, growth and interaction of deformation-induced α'' martensite in metastable Ti−10V−2Fe−3Al [J]. Materials Science and Engineering A, 2021, 802: 140237.

[6] COTTON J D, BRIGGS R D, BOYER R R, TAMIRISAKANDALA S, RUSSO P, SHCHETNIKOV N, FANNING J C. State of the art in beta titanium alloys for airframe applications [J]. JOM, 2015, 67(6): 1281−1303.

[7] ZHU Wen-guang, LEI Jia, ZHANG Zhi-xin, SUN Qiao-yan, CHEN Wei, XIAO Lin, SUN Jun. Microstructural dependence of strength and ductility in a novel high strength β titanium alloy with Bi-modal structure [J]. Materials Science and Engineering A, 2019, 762: 138086.

[8] ZHAO Shuai, WANG Yang, PENG Lin, ZHANG Yuan-xiang, RAN Rong, YUAN Guo. Effect of annealing temperature on microstructure and mechanical properties of cold-rolled commercially pure titanium sheets [J]. Transactions of Nonferrous Metals Society of China, 2022, 32(8): 2587−2597.

[9] IVANOV A, ORLOV A, GOLUBOVSKII E. The influence of thermomechanical processing on the structure and mechanical properties of rods made of high-strength titanium alloys of different classes [J]. Materials Today: Proceedings, 2019, 19: 2163−2166.

[10] ZHAO Qin-yang, SUN Qiao-yan, XIN She-wei, CHEN Yong-nan, WU Cong, WANG Huan, XV Jian-wei, WAN Ming-pan, ZENG Wei-dong, ZHAO Yong-qing. High-strength titanium alloys for aerospace engineering applications: A review on melting-forging process [J]. Materials Science and Engineering A, 2022, 845: 143260.

[11] SRINIVASU G, NATRAJ Y, BHATTACHARJEE A, NANDY T K, NAGESWARA RAO G V S. Tensile and fracture toughness of high strength β Titanium alloy, Ti−10V−2Fe−3Al, as a function of rolling and solution treatment temperatures [J]. Materials & Design, 2013, 47: 323−330.

[12] MA Xin-kai, CHEN Zhuo, XIAO Lei, LUO Shi-feng, LU Wen-jie. Stress-induced martensitic transformation in a β-solution treated Ti−10V−2Fe−3Al alloy during compressive deformation [J]. Materials Science and Engineering A, 2021, 801: 140404.

[13] ZHANG Jin-hu, JU Hong-tao, XU Hai-sheng, YANG Liang, MENG Zhi-chao, LIU Chen, SUN Ping, QIU Jian-ke, BAI Chun-guang, XU Dong-sheng, YANG Rui. Effects of heating rate on the alloy element partitioning and mechanical properties in equiaxed $\alpha+\beta$ Ti−6Al−4V alloy [J]. Journal of Materials Science & Technology, 2021, 94: 1−9.

[14] ZHANG Hong-yu, ZHANG Ya-ran, LIANG Hong-yan, LIU Yong-chang. Influence of cooling rates on microstructure and tensile properties of a heat treated Ti2AlNb-based alloy [J]. Materials Science and Engineering A, 2021, 817: 141345.

[15] DA COSTA TEIXEIRA J, APPOLAIRE B, AEBY-GAUTIER E, DENIS S, CAILLETAUD G, SPÄTH N. Transformation kinetics and microstructures of Ti17 titanium alloy during continuous cooling [J]. Materials Science and Engineering A, 2007, 448(1/2): 135−145.

[16] WU Hui-li, SUN Zhi-chao, CAO Jing, YIN Zhi-kun. Diffusion transformation model in TA15 titanium alloy: The case of nonlinear cooling [J]. Materials & Design, 2020, 191: 108598.

[17] MAHENDER T, ANANTHA PADMANABAN M R, BALASUNDAR I, RAGHU T. On the optimization of temperature and cooling rate to maximize strength and ductility of near α titanium alloy IMI 834 [J]. Materials Science and Engineering A, 2021, 827: 142052.

[18] WU Cong, ZHAO Yong-Qing, HUANG Shi-xing, SUN Qiao-yan, ZHOU Lian. Effect of cooling rate on α variant selection and microstructure evolution in a near β Ti−5Al−3Mo−3V−2Cr−2Zr−1Nb−1Fe alloy [J]. Journal of Alloys and Compounds, 2020, 841: 155728.

[19] SUN Zhi-chao, GUO Shuang-shuang, YANG He. Nucleation and growth mechanism of α-lamellae of Ti alloy TA15 cooling from an $\alpha+\beta$ phase field [J]. Acta Materialia, 2013, 61(6): 2057−2064.

[20] TANG Bin, KOU Hong-chao, ZHANG Xue, GAO Pu-yi, LI Jin-shan. Study on the formation mechanism of α lamellae in a near β titanium alloy [J]. Progress in Natural Science: Materials International, 2016, 26(4): 385−390.

[21] WANG Kai-ge, WU Di, WANG Dong, DENG Zi-xuan, TIAN Yue-yan, ZHANG Li-gang, LIU Li-bin. Influence of cooling rate on ω phase precipitation and deformation mechanism of a novel metastable β titanium alloy [J]. Materials Science and Engineering A, 2022, 829: 142151.

[22] XIAO J F, NIE Z H, TAN C W, ZHOU G, CHEN R, LI M R, YU X D, ZHAO X C, HUI S X, YE W J, LEE Y T. Effect of reverse β-to-ω transformation on twinning and martensitic transformation in a metastable β titanium alloy [J]. Materials Science and Engineering A, 2019, 759: 680−687.

[23] BARRIOBERO-VILA P, REQUENA G, WARCHOMICKA F, STARK A, SCHELL N, BUSLAPS T. Phase transformation kinetics during continuous heating of a

β-quenched Ti−10V−2Fe−3Al alloy [J]. Journal of Materials Science, 2015, 50(3): 1412−1426.

[24] LEE S W, LEE H J, KIM J H, PARK C H, HONG J K, YEOM J T. Effect of prior *β* grain size on the martensitic transformation of titanium alloys [J]. Materials Characterization, 2021, 182: 111525.

[25] LIU C M, WANG H M, TIAN X J, LIU D. Development of a pre-heat treatment for obtaining discontinuous grain boundary *α* in laser melting deposited Ti−5Al−5Mo−5V−1Cr−1Fe alloy [J]. Materials Science and Engineering A, 2014, 604: 176−182.

[26] DONG Yue, LIU Xin-gang, ZOU Jun-jie, KE Yu-jiao, LIU Peng-wei, MA Lan, LUO Heng-jun. Effect of cooling rate following *β* forging on texture evolution and variant selection during *β*→*α* transformation in Ti-55511 alloy [J]. Journal of Materials Science & Technology, 2022, 113: 1−13.

[27] ZHANG J Y, LI J S, CHEN Z, MENG Q K, SUN F, SHEN B L. Microstructural evolution of a ductile metastable *β* titanium alloy with combined TRIP/TWIP effects [J]. Journal of Alloys and Compounds, 2017, 699: 775−782.

[28] ELLYSON B, KLEMM-TOOLE J, CLARKE K, FIELD R, KAUFMAN M, CLARKE A. Tuning the strength and ductility balance of a TRIP titanium alloy [J]. Scripta Materialia, 2021, 194: 113641.

[29] ALI T, WANG Lin, CHENG Xing-wang, CHENG Huan-wu, YANG Ying, LIU An-jin, XU Xue-feng, ZHOU Zhe, NING Zi-xuan, XU Zi-qi, MIN Xin-hua. Mechanical (compressive) form of driving force triggers the phase transformation from *β* to *ω* & *α*″ phases in metastable *β* phase-field Ti-5553 alloy [J]. Journal of Materials Science & Technology, 2021, 78: 238−246.

[30] JUN J H, CHOI C S. Variation of stacking fault energy with austenite grain size and its effect on the M_S temperature of *γ*→*ε* martensitic transformation in Fe−Mn alloy [J]. Materials Science and Engineering A, 1998, 257(2): 353−356.

[31] APPOLAIRE B, HÉRICHER L, AEBY-GAUTIER E. Modelling of phase transformation kinetics in Ti alloys–Isothermal treatments [J]. Acta Materialia, 2005, 53(10): 3001−3011.

[32] WANG Shu, LIANG Yi-long, SUN Hao, FENG Xin, HUANG Chao-wen. Thermomechanical treatment-induced microstructure refinement to optimize mechanical properties of TC21 titanium alloys [J]. Materials Science and Engineering A, 2021, 812: 141095.

[33] WANG B B, XIE G M, WU L H, XUE P, NI D R, XIAO B L, LIU Y D, MA Z Y. Grain size effect on tensile deformation behaviors of pure aluminum [J]. Materials Science and Engineering A, 2021, 820: 141504.

[34] LI Si-yun, ZHANG Lei, ZHANG Ya-cen, YANG Qi, LIU Hui-qun, ZHANG Xiao-yong. Coherent *ω* phase induced yield strength improvement in Ti−19Nb−1.5Mo−4Zr−8Sn alloy [J]. Results in Physics, 2020, 19: 103366.

[35] TAN Chang-sheng, SUN Qiao-yan, XIAO Lin, ZHAO Yong-qing, SUN Jun. Slip transmission behavior across *α*/*β* interface and strength prediction with a modified rule of mixtures in TC21 titanium alloy [J]. Journal of Alloys and Compounds, 2017, 724: 112−120.

Ti-1023 合金自 *β* 相区慢冷过程中的显微组织演变及力学性能

明 惠，朱程鹏，宋雪雁，张晓泳，周科朝

中南大学 粉末冶金国家重点实验室，长沙 410083

摘 要：系统研究 Ti-1023 合金在以 1 ℃/min 的冷却速度从单相区冷却到两相区的过程中的显微组织演变和力学性能。随着最终冷却温度的降低，在 *β* 基体上依次析出晶界 *α*′马氏体(α'_{GB})、晶界 *α* 相(α_{GB})、魏氏体晶界 *α* 相(α_{WGB})和魏氏体晶内 *α* 相(α_{WI})。相应地，Ti-1023 合金的力学性能和变形机制也发生了显著变化。当最终冷却温度高于 700 ℃时，拉伸曲线出现明显的双屈服现象，并且伸长率大于 20%。而最终冷却温度低于 700 ℃时，双屈服现象消失。这主要是由于随着 *α*(*α*′)析出相的增加，Ti-1023 合金的 *β* 稳定性增强，其室温变形机制逐渐从应力诱导的 *α*″马氏体相变转变为位错滑移。此外，结合晶粒尺寸和析出相效应，分析 Ti-1023 合金的强化机制。

关键词：Ti-1023 合金；显微组织演变；晶界 *α*′马氏体；热处理

(Edited by Xiang-qun LI)